

Segmented Swing-Structured Fur-Based Triboelectric Nanogenerator for Harvesting Blue Energy toward Marine Environmental Applications

Hao Pang, Yawei Feng, Jie An, Pengfei Chen, Jiajia Han, Tao Jiang,*
and Zhong Lin Wang*

Reducing carbon emissions to realize carbon neutrality is crucial to the environmental protection, and developing clean and renewable energy sources is an effective means to achieve this goal. Triboelectric nanogenerators (TENGs) provide a promising energy technology for converting the abundant renewable ocean wave energy on the earth surface. In this work, a segmented swing-structured fur-based TENG (SSF-TENG) is designed and fabricated to harvest low frequency water wave energy. The introduction of soft and dense rabbit furs reduces the frictional resistance and material wear, and the design and optimization of segmented structures further enhance the output performance of TENG. The use of ultra-lubricated bearings makes the SSF-TENG achieve an extended period of energy harvesting of more than 5 min after one triggering, with a total energy conversion efficiency of up to 23.6%. Under the real water wave triggering, the SSF-TENG can deliver a maximum peak power of 6.2 mW and an average power of 0.74 mW. Furthermore, through effective water wave energy harvesting by the SSF-TENG or array, self-powered marine environmental applications are successfully demonstrated, which establishes a solid foundation for large-scale blue energy harvesting and realization of smart oceans.

prospects in the fields of marine information acquisition and environmental monitoring toward smart oceans.^[2,3] So, much attention has been attracted from worldwide researchers on water wave energy harvesting on a large scale. Current converters of wave energy mainly rely on the electromagnetic generator (EMG).^[4,5] However, the energy conversion efficiency of EMG at the low frequency of water waves is very low due to the low output voltage, limiting its practical applications. Therefore, it is very necessary to develop new efficient harvesting technologies and devices suitable for the low-frequency wave energy.

Triboelectric nanogenerator (TENG, also called as Wang generator) has been widely applied to capture various forms of ambient mechanical energy, such as human activity,^[6,7] mechanical vibration,^[8] wind,^[9] and water wave energies,^[10,11] etc. The TENG adopting the mechanism

of Maxwell's displacement current^[12,13] is based on the coupling of triboelectrification and electrostatic induction.^[14–17] Compared to traditional EMG, the TENG shows the advantages of lightweight, low cost, and high efficiency, and it provides a subversive technological path for efficient water wave energy harvesting.^[18,19] So far, a variety of TENG structures have been designed to collect water wave energy, and then TENG networks by integration of multiple units have been

1. Introduction

Carbon emission reduction has become a crucial issue for the world community,^[1] which can be achieved by exploiting renewable energy sources. Ocean contains abundant and clean renewable blue energy, including ocean wave energy, tidal energy, and so on. As the key direction of ocean energy development, the harvesting of ocean wave energy exhibits broad application

H. Pang, T. Jiang
School of Chemistry and Chemical Engineering
Guangxi University
Nanning, Guangxi 530004, P. R. China
E-mail: jiangtao@binn.cas.cn

H. Pang, Y. Feng, J. An, P. Chen, J. Han, T. Jiang, Z. L. Wang
CAS Center for Excellence in Nanoscience
Beijing Key Laboratory of Micro-Nano Energy and Sensor
Beijing Institute of Nanoenergy and Nanosystems
Chinese Academy of Sciences
Beijing 101400, P. R. China
E-mail: zlwang@gatech.edu

Y. Feng, J. An, P. Chen, J. Han, T. Jiang, Z. L. Wang
School of Nanoscience and Technology
University of Chinese Academy of Sciences
Beijing 100049, P. R. China

T. Jiang, Z. L. Wang
CUSTech Institute
Wenzhou, Zhejiang 325024, P. R. China
Z. L. Wang
School of Materials Science and Engineering
Georgia Institute of Technology
Atlanta, GA 30332-0245, USA

 The ORCID identification number(s) for the author(s) of this article can be found under <https://doi.org/10.1002/adfm.202106398>.

DOI: 10.1002/adfm.202106398

constructed for larger-scope wave energy conversion.^[20,21] For a common contact-separation TENG, its output performance will be reduced after long-time operation due to the material wear, while the surface triboelectric charges for a non-contact freestanding TENG can gradually attenuate without the charge supplement. In previous works,^[22,23] a kind of swing-structured TENG with soft-contact dielectric brush design was found to possess improved performance, durability, and high energy conversion efficiency in harvesting low-frequency water wave energy. The swing structure can realize multiplied output frequency by elongating the operation time after one triggering. Nevertheless, the output current of such TENG is still low due to the non-optimal triboelectric pair, and the swing time is not long enough for the resistance from the material friction and bearings. Therefore, further structural optimization is desirable for the TENG to achieve higher output performance and stronger durability, as well as benefiting for the large-scale networking integration of TENG units.

In the present work, the swing-structured TENG was further optimized by using the flexible rabbit fur brushes and segmented structure, which effectively extended the time period of energy harvesting, the lifetime of TENG, and thus the total energy conversion efficiency. The softer rabbit furs with strong electropositivity could reduce the friction resistance between triboelectric materials to achieve higher outputs,^[24] and ultra-lubricated ceramic bearings were adopted to further elongate the swing time after one triggering. First, the output performance of the segmented swing-structured fur-based TENG (SSF-TENG) with various segmented structures was systematically measured under the regular triggering. The efficiency and durability of the TENG were also revealed. Subsequently, in real water wave tests, the influence of water wave conditions on the SSF-TENG performance was further explored. Finally, an

array composed of four SSF-TENG units was constructed to demonstrate the applications of self-powered marine environment information monitoring and metal anti-corrosion through harvesting low-frequency blue energy.

2. Results and Discussion

The cylindrical swing-structured TENG with four groups of flexible rabbit fur brushes and internal segmented structure was designed, as schematically shown in **Figure 1a**. The outside shell of the SSF-TENG, made of UV-curable resins, is fabricated by using 3D printing technology. Two stiffeners are added to the shell to enhance its strength and prevent deformation. Rabbit fur brushes are placed inside four hollow strips designed on the shell, instead of being adhered to on the internal wall to hinder the swing movement. The swing component with segmented structure is also made by 3D printing technology, and polytetrafluoroethylene (PTFE) films are attached to the surfaces of its protuberant part for electrostatic induction. As can be seen from the enlarged view, there is an air gap of 1.5 mm between the swing component and the complementary electrodes. Four copper blocks are added onto the bottom of the swing component as a counterweight to lower the center of gravity, benefiting the swing movement under external excitation. The rabbit fur brushes can supplement the charges by rubbing with the PTFE films with low frictional resistance. The flexible copper electrodes manufactured by printed circuit board (PCB) technology are adhered onto the inner wall of the shell to form an integrated freestanding TENG with multiple units connected in parallel. In addition, ultra-lubricated ceramic bearings between the steel shaft and swing component were adopted to further reduce the frictional resistance. The photograph of the as-fabricated SSF-TENG device is shown in **Figure 1b**.

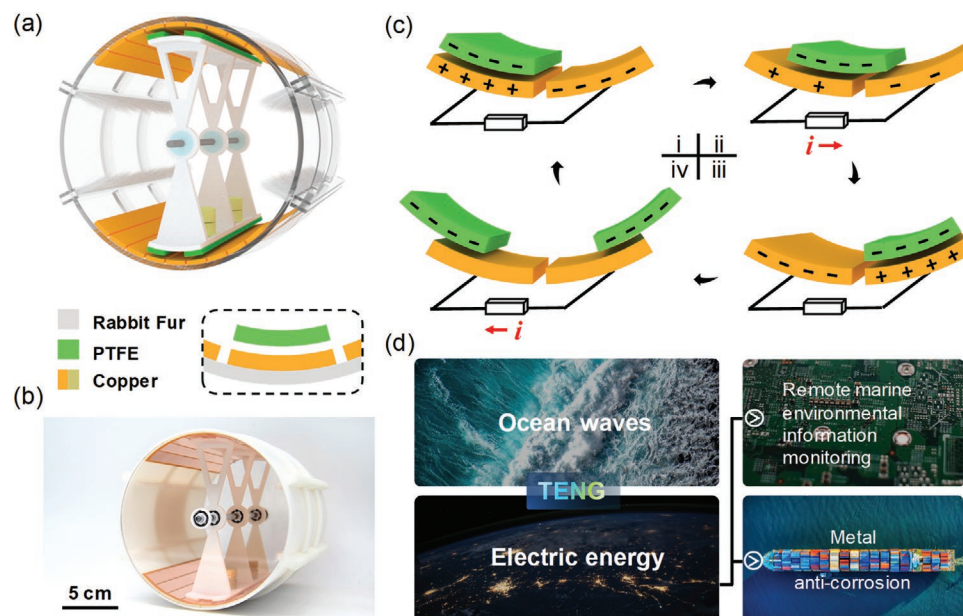


Figure 1. Structure, working principle, and application of the segmented swing-structured fur-based TENG. a) 3D overview of the structure and material composition of the SSF-TENG, where a partially enlarged view shows an air gap of 1.5 mm between the swing component and the complementary electrodes. b) Photograph of the as-fabricated SSF-TENG device. c) Schematic working principle for one basic unit of the SSF-TENG. d) Schematic diagram of smart oceans realized by constructing self-powered marine environmental application systems.

The working process of the SSF-TENG is based on the coupling of triboelectrification and electrostatic induction. Under an external triggering, the swing component will swing left and right, and rub against the rabbit fur brushes, generating positive charges on the rabbit furs and negative charges on the PTFE surfaces. The negative charges on the PTFE are gradually accumulated to achieve saturation after several cycles. The next process is the electrostatic induction, which is schematically shown in Figure 1c. Only one basic unit is presented for clarifying the working principle. At the initial state, the grating PTFE strips on the swing component are aligned with the grating electrodes (Figure 1c-i), and an equal amount of opposite charges are induced on the two electrodes. Then the applied external triggering drives the swing component to swing rightward (Figure 1c-ii), which makes free electrons flow from the right to the left electrode through the external circuit. The induced current direction from the left to the right electrode is maintained until the PTFE gets matched with the right

electrode (Figure 1c-iii). When the swing component moves further, free electrons flow reversely, and a reversed current is generated (Figure 1c-iv). During one swing period, the segmented TENG can produce alternating current outputs of multiple cycles. Figure 1d shows a schematic diagram of smart oceans realized by constructing self-powered marine environmental application systems. The large-scale ocean wave energy can be harvested by the TENG devices and converted to electric energy for powering marine environmental information detection and metal anti-corrosion systems. Assisted by the power management and storage, the environmental information sensors can be stably powered, and the detected data can be wirelessly transmitted to the receiving center or data processing center for realizing remote marine environmental monitoring. The whole process does not need an external power supply.

The output characteristics of the improved SSF-TENG without segmented structure were investigated under the regular triggering of linear motor. Figure 2a shows the comparison

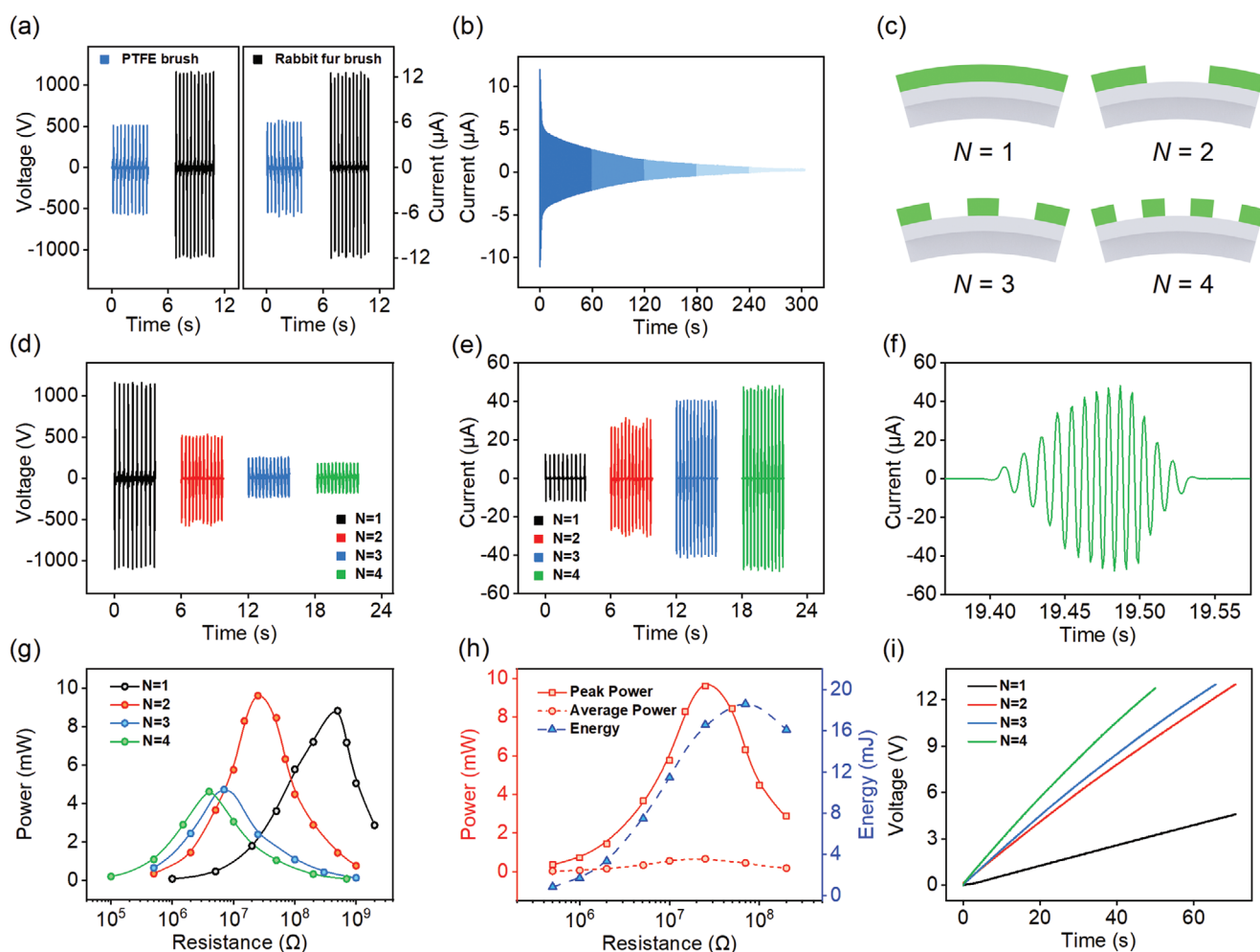


Figure 2. Influence of rabbit fur brush and segmented structure on the output performance of SSF-TENG. a) Comparison of output voltage and current of the swing-structured TENG without segmented structure using rabbit hair brushes and PTFE brushes. b) Output current profile of the SSF-TENG showing the swing time after one triggering. c) Schematic diagrams of the segmented structures with various grating numbers. d) Output voltage and e) output current for different segmented structures. f) Enlarged output current curve for $N = 4$ during one swing period. g) Peak output power-resistance relationship at $N = 1-4$. h) Peak output power, average output power-resistance relationships under continuous triggering, and translated energy-resistance relationship under one triggering for $N = 2$. i) Charging voltage on the $22 \mu\text{F}$ capacitor for the SSF-TENGs with different N .

of output voltage and current between the improved TENG and the previous one,^[20] using the rabbit fur brushes and PTFE brushes, respectively. The size of swing component, triggering conditions of linear motor (maximum displacement $s = 7$ cm, acceleration $a = 75$ m s⁻²), and other parameters were kept the same. It can be seen that the voltage increases from 572 to 1160 V, and the current rises from 6.3 to 12.6 μ A, as well as the improvement from 195.0 to 239.6 nC for the transferred charge (Figure S1, Supporting Information). The resistance of the swing component motion in such structure mainly comes from the bearings, and when using the ultra-lubricated ceramic bearings, the frictional resistance can be further reduced significantly. As shown in Figure 2b, the oscillation can be sustained for more than 5 min after one single external triggering (Video S1, Supporting Information). Subsequently, the segmented structure was designed for both the swing component and the copper electrodes, aiming to elevate the output current. The schematic diagrams of the segmented structures with various grating numbers are shown in Figure 2c. The grating number N denotes the number of the protuberant units on each arch-shaped part of the swing component with a fixed central angle of 30°. The protuberant units having the consistent size with each electrode unit are alternate with the concave units. For $N = 2, 3$, and 4, the corresponding central angles for one protuberant unit were designed as 9.47°, 5.735°, and 3.983°, respectively, to ensure the unchanged electrode area of 218.5 cm² adhered onto the inner wall.

Figure 2d,e illustrates the output characteristics for different segmented structures. The maximum outputs are obtained at the motor parameters of $s = 3$ cm and $a = 8$ m s⁻² for grating numbers $N = 2, 3$, and 4. The detailed results regarding the influences of the motor conditions on the electric outputs are shown in Figure S2, Supporting Information. With increasing the grating number, the output voltage gradually decreases, while the output current increases. When the N increases to 4, the voltage and current arrive at 188.6 V and 48.0 μ A. Besides, the transferred charge gradually decreases (Figure S3, Supporting Information), which is attributed to the decrease of triboelectric charge amount with the increase of grating number. Only the protuberant units are attached by PTFE films, and the total area of protuberant parts decreases. Meanwhile, during one swing period, more output current cycles can be observed for larger N . The current peak numbers for $N = 1-4$ during one swing period are respectively 2, 10, 18, and 26 (Figure S4, Supporting Information, Figure 2f), satisfying the relation of $8N-6$. It implies that the total translated charge within one swing period is higher at larger N .

The resistive load behaviors of the SSF-TENG with different N were systematically studied. Figure 2g shows the peak output power of the TENG with respect to the N , indicating the highest peak output power of 9.6 mW can be achieved for the optimal grating number of 2. Also it can be found that the matched resistance decreases with the grating number, because of the increase of the TENG capacitance for finer electrodes. The peak output power, average output power-resistance relationships under continuous triggering, and translated energy-resistance relationship under one triggering for the SSF-TENG with $N = 2$ are presented in Figure 2h. The average power can be obtained by the harvested energy per unit time, and the

harvested energy during one triggering can be calculated by the following equation

$$E = \int I(t)^2 R dt \quad (1)$$

where the $I(t)$ is the current across the resistor at the time t , and R is the resistance. Under the performed conditions, the maximum peak power of 9.6 mW at 25 M Ω , maximum average power of 0.67 mW at 25 M Ω , and the maximum energy of 18.6 mJ at 70 M Ω can be delivered. In addition, the charging performances of the TENGs with different N to a fixed capacitor of 22 μ F were compared, as shown in Figure 2i. The increase in the grating number can raise the charging speed, and the capacitor is charged to 13 V within 50 s at $N = 4$.

In Figure 2, we constructed the segmented structure to enhance the output current at the fixed total size of the swing component. The protuberant and concave units on the swing component need to appear alternately for enabling the normal operation of SSF-TENG, leading to the decreases of effective tribo-surface area and triboelectric charge amount. Figure 3a shows the 3D schematic diagram of swing component structure, and the central angles of the three swing components are all 30° at $N = 1, 2$, and 4 (Figure 3a-i-iii). To ensure the same effective tribo-surface area (the green regions) as the non-segmented structure, a larger size of swing components were fabricated, based on the cases of $N = 2$ and 4, which are denoted by $N = 2+$ and $4+$ (Figure 3a-iv,v). When adjusting the swing component size, the induced electrodes were kept unchanged. The cases of $N = 2$ and 4 were chosen as examples, because the maximum peak power is achieved at $N = 2$ and the charging speed is the fastest at $N = 4$. Then the following experiments will mainly focus on these two segmented structures of $N = 2+$ and $4+$.

First, the amounts of transferred charges for the modified segmented structures of $N = 2+$ and $N = 4+$ were measured and compared with the cases of smaller swing components at $N = 2$ and 4, as illustrated in Figure 3b. The maximum transferred charges were found to greatly increase, from 208.4 to 308.0 nC for the transition from $N = 2$ to $N = 2+$, while from 124.5 to 199.9 nC for that from $N = 4$ to $N = 4+$. The transferred charges get the maximum values under the motor conditions of $s = 3$ cm, $a = 8$ m s⁻² for $N = 2+$, and $s = 7$ cm, $a = 7$ m s⁻² for $N = 4+$. The results indicate that the increase of effective tribo-surface area can indeed increase the amount of transferred charges. Also, the output current of the SSF-TENG can be further improved by increasing the swing component size, as shown in Figure 3c. The output current for $N = 4+$ can reach 74.0 μ A, which is 10.7 times higher than the 6.3 μ A of the previous work,^[20] and the output voltage is also significantly improved (Figure S5, Supporting Information).

The resistive load behavior of the modified SSF-TENG was also investigated to compare with that of the initial SSF-TENG. Figure 3d shows the comparison of the peak output power for the TENGs of $N = 2$ and $N = 2+$, indicating that when increasing the effective tribo-surface area, the peak power increases significantly from 9.6 to 16.3 mW by 70.0%. The power improvement from $N = 4$ to $N = 4+$ is even more obvious, from 4.6 to 11.2 mW by 143.5% (Figure S6, Supporting Information). The matched resistance of the modified TENG remains the same,

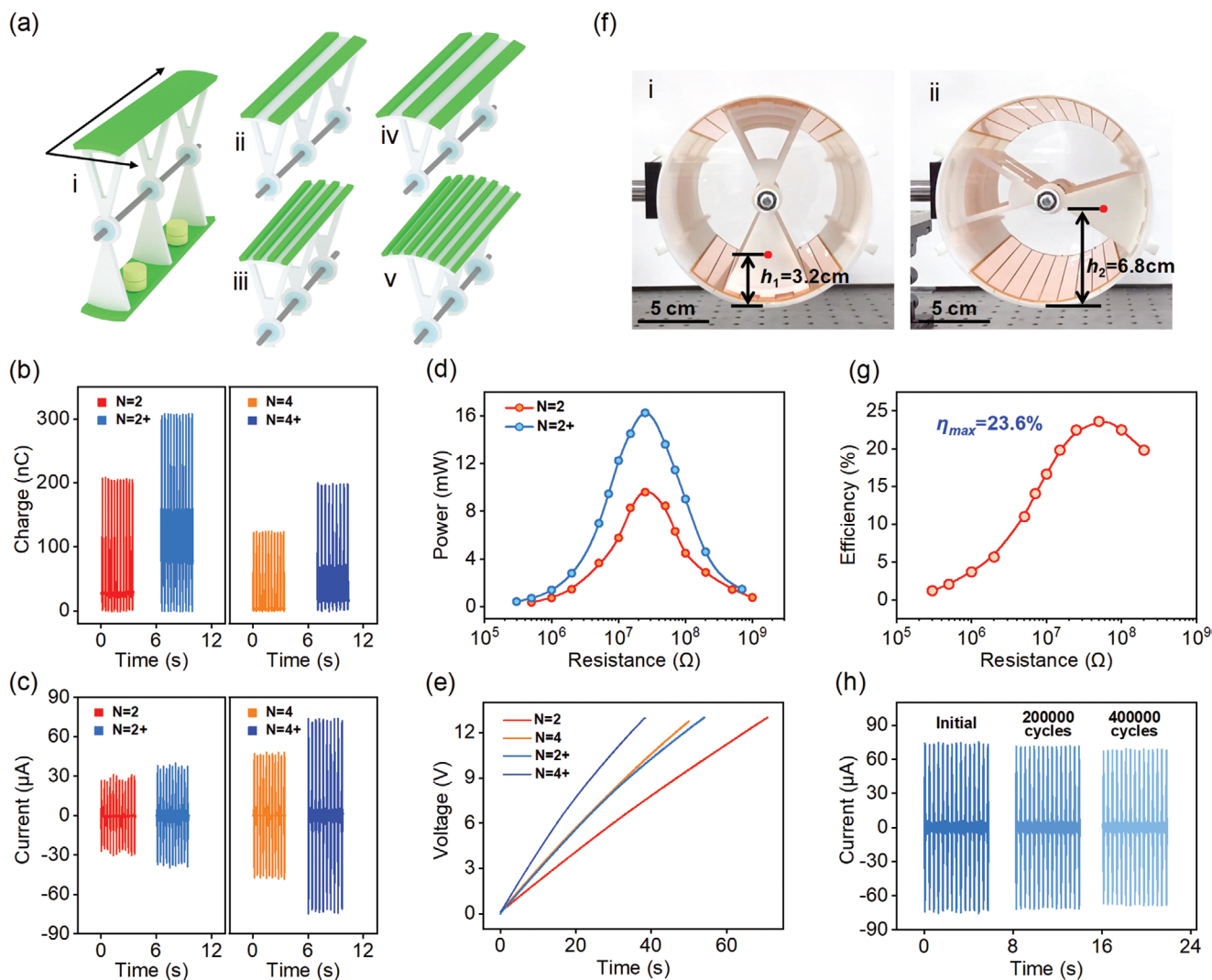


Figure 3. Optimization of segmented structure and performance investigation. a) 3D schematic diagram of swing component structure. The central angles of the swing components are 30° at $N = 1, 2, 4$ (i–iii), and the same effective tribo-surface area (the green regions) as the non-segmented structure is kept at $N = 2+$ and $4+$ (iv–v). (b,c) Comparison of b) transferred charge and c) output current of the segmented structures at $N = 2, 2+, 4, 4+$. d) Comparison of peak output power-resistance relationship at $N = 2, 2+, 4, 4+$. e) Charging voltage curves for the segmented structures at $N = 2, 2+, 4, 4+$. f) Photographs of the swing component states showing different centers of gravity at the initial state (i) and highest state (ii) for the SSF-TENG with $N = 2+$. g) Energy conversion efficiency with respect to the load resistance at $N = 2+$. h) Durability of the SSF-TENG device when testing for various cycles.

because of the unchanged TENG capacitance from the constant electrodes, although the swing component becomes larger. The peak power, average power under stable triggering, and the energy output after one trigger with respect to the resistance for $N = 2+$ are shown in Figure S7, Supporting Information. Maximum average power of 1.8 mW at 25 MΩ, and maximum energy of 19.6 mJ at 50 MΩ are delivered. Besides, the charging speed of the modified TENGs to a capacitor is also enhanced, as shown in Figure 3e. For the fastest charging speed at $N = 4+$, it takes 38.4 s to charge a 22 μF capacitor to 13 V, saving 11.6 s compared to the case of $N = 4$.

Subsequently, the energy conversion efficiency of SSF-TENG under one triggering was evaluated. The external impact makes the internal swing component oscillate from side to side, converting the mechanical energy into electric energy. Therefore, the energy conversion efficiency can be obtained by the ratio

of the output electric energy after one triggering to the gravitational potential energy difference between the maximum swing state and the initial state, which is given by

$$\eta = \frac{E_{\text{output}}}{E_{\text{input}}} = \frac{\int I(t)^2 R dt}{mg(h_2 - h_1)} \quad (2)$$

where $I(t)$ is the output current across the load resistance R , m is the total mass of swing component, g is the acceleration of gravity, and h_1, h_2 are the heights between the center of gravity and the cylinder shell bottom at the initial state and the maximum swing state, which can be obtained by capturing the movement states of swing component by a camera. Figure 3f shows the photographs of the two states for the SSF-TENG with $N = 2+$. Through calculation, the maximum energy conversion efficiency of $N = 2+$ can reach up to 23.6%, as presented

in Figure 3g. The motion state photographs and energy conversion efficiency of other segmented structures are presented in Figures S8, Supporting Information. Note that although the output performance of SSF-TENG is significantly enhanced, the energy conversion efficiency is not improved. That is mainly ascribed to the use of UV-curable resins, which reduces the weight of the swing component. The total mass of the swing components with $N = 2, 2+, 4,$ and $4+$ are 201.2, 235.4, 195.6, and 248.0g, respectively, which are 26.2%, 13.7%, 28.3%, and 9.1% less than that in the previous work (272.8g). So the center of gravity is lowered, and the swing component can oscillate to a higher height, leading to a significant increase in gravitational potential energy.

The durability test result of the SSF-TENG is shown in Figure 3h, taking the segmented structure of $N = 4+$ as an example. It can be observed that after continuous triggering of 400 000 cycles by the linear motor, the output current only has a slight decrease, indicating the excellent durability of the SSF-TENG. The reasons why such TENG can achieve better durability than other TENGs are described as follows. The non-contact electrostatic induction and soft-contact of the PTFE surfaces with the rabbit fur brushes can greatly reduce the material wear of the PTFE. And also the rabbit furs can continuously replenish the triboelectric charges for the PTFE.

From the above experimental results under the regular triggering, the maximum peak output power is achieved at $N = 2+$, because of its larger matched resistance than that at $N = 4+$. Actually, the output current of $N = 4+$ is the largest and its charging speed to a capacitor is the fastest, which is more in line with the requirements of practical applications. Therefore,

the segmented structure of $N = 4+$ was selected as a representative structure to measure the output performance of SSF-TENG under real water wave triggering.

Similar to our previous work,^[25] a water wave generator was used to simulate the real water wave environment in a water tank, and the water wave frequency is controlled by the dwell time of the rotational motor. The detailed measurement method can be found in the Experimental Section. Previous works all show that the electrical outputs of TENG increase with increasing the water wave height.^[25,26] Therefore, in this work, the influence of water wave frequency on the outputs of SSF-TENG was mainly explored, and the wave height was set as 10 cm. Figure 4a and Figure S9, Supporting Information, show the output current, voltage, and transferred charge of the SSF-TENG device at various water wave frequencies. Under the real water wave triggering, the SSF-TENG produces the maximum outputs of 59.9 μA , 300 V, and 284.4 nC at the optimal frequency of 1.1 Hz. Similar to the previous phenomenon, the transferred charge generated in the water waves is larger than that on the linear motor, indicating that the SSF-TENG has a greater amplitude of motion under the impact of the real water waves.

The swing time of the SSF-TENG in the water after one triggering is also prolonged, which lasts for about 130 s, as shown in Figure 4b. The extension of the swing time can greatly increase the output energy and energy conversion efficiency of SSF-TENG, making it very suitable for harvesting ultra-low frequency water wave energy. Then at the optimal water wave frequency of 1.1 Hz, the charging performance of the SS-TENG to different capacitors was measured. As presented in Figure 4c,

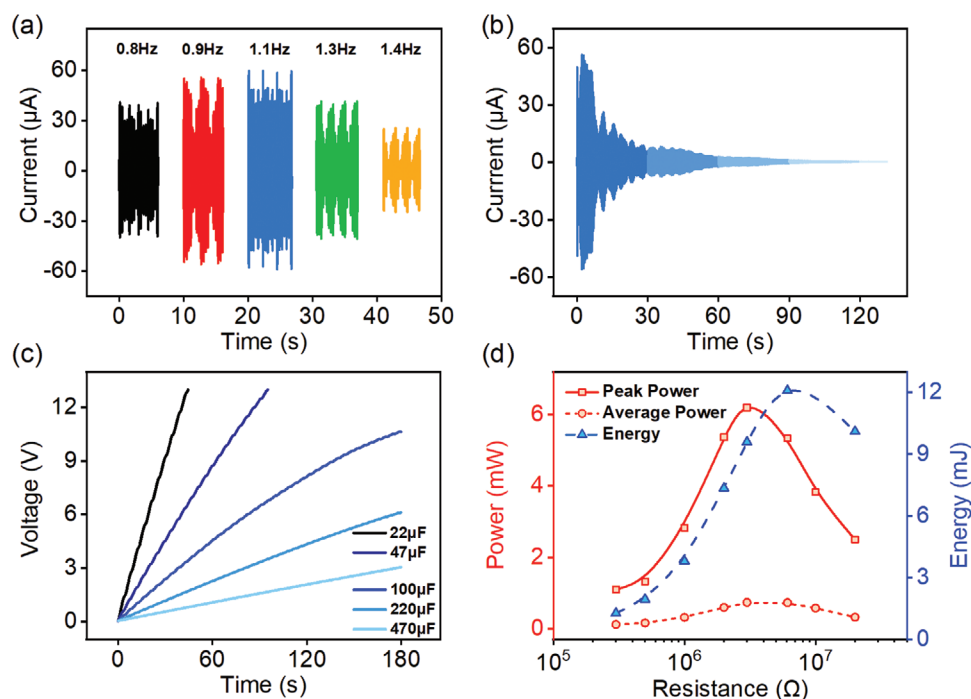


Figure 4. Output performance of one SSF-TENG device under water wave triggering at a fixed water wave height of 10 cm. a) Influence of the water wave frequency on the output current of the SSF-TENG. The optimal wave frequency is 1.1 Hz. b) Output current profile showing the swing time of SSF-TENG after one water wave triggering. c) Charging voltage on various capacitances for the SSF-TENG. d) Peak power, average power under stable water wave triggering, and translated energy after one triggering as functions of the load resistance for the SSF-TENG.

the charging speed of SSF-TENG is significantly improved compared to the previous work. The charging voltage on the 470 μF capacitor can arrive at 3.04 V within 180 s, corresponding to 1.43 mC of output charge, which is an improvement of 4.8 times. Moreover, the resistance-dependent output performance of the SSF-TENG of $N = 4+$ at the wave frequency of 1.1 Hz was measured, as shown in Figure 4d. The peak output power, average power, and translated energy of the SSF-TENG can be calculated to be 6.2 mW (improved by 11.1 times), 0.74 mW (improved by 7.0 times), and 12.1 mJ (improved by 4.6 times), respectively. The corresponding matched load resistances are respectively 3, 3, and 6 $\text{M}\Omega$. According to the device volume, the peak power density and average power density are obtained to be 1.75 and 0.21 W m^{-3} , respectively.

To realize large-scale ocean wave energy harvesting, multiple TENG units need to be connected into an array or network. Consequently, the output and charging performances of the TENG array or network need to be systematically measured. In this work, four SSF-TENG units were integrated into an array as an example. To ensure the synchronous motions of all TENG units in the array, they were placed in a sealed acrylic box, which can also increase the air gap between the electrodes and water surfaces to diminish the dielectric shielding of the water. As can be seen from Figure 5a,b, at the optimal frequency of 1.1 Hz, the output current and voltage of a single TENG decrease slightly. This is because placing the SSF-TENGs into the acrylic box weakens the impact force of water waves, and thus affects the swing motion of SSF-TENGs. As the number of TENG units connected in parallel within the array increases, the current is almost continuously superimposed. The output current for the TENG array with 4 units can reach 120.3 μA , while the voltage is basically unchanged. The results show that a larger output current can be achieved by connecting more TENG units, exhibiting important practical application values.

Figure 5c shows the charging performance of the array with different TENG units to a 22 μF capacitor. With the increase in the unit number, the charging speed increases gradually. The

4-unit array can charge the capacitor to 13 V in 14.1 s, which corresponds to an output charge of 286 μC . And also the peak output power for different units on resistive loads was calculated in Figure 5d, showing that the maximum peak power is 8.8 mW at 3 $\text{M}\Omega$ for 4 units. The matched resistance is slightly decreased with increasing the unit number, resulting from the capacitance increase. Figure 5e shows the typical output power-resistance relationship under stable triggering and energy-resistance relationship under one triggering for the TENG array with 4 units. The average power of 1.0 mW at 3 $\text{M}\Omega$ and translated energy of 21.3 mJ at 6 $\text{M}\Omega$ are obtained. The typical charging voltage profiles to various load capacitors from 22 to 470 μF for 4 units, as plotted in Figure 5f, show that a 470 μF capacitor can be charged to 2.93 V in 60 s, delivering an output charge of 1.38 mC.

Changes in the marine environment have significant impacts on human production and life, so it is very necessary to monitor the marine environment. The TENGs have played important roles in constructing self-powered marine environmental application systems toward smart oceans. Figure 6a shows the photograph of a remote marine environmental information monitoring system driven by an array of four SSF-TENGs through the water wave energy harvesting. Assisted by the rectification and storage circuit, the transmitter and temperature/humidity sensor can be powered, detecting the temperature and humidity at the water surface, and sending the data to the computer with the receiver, for self-powered marine environmental information monitoring. As shown in Figure 6b, under the water wave conditions of 10 cm and 1.1 Hz, the capacitor of 470 μF is charged to 5.0 V within 109 s. When the switch is closed, the receiver acquires the temperature/humidity data, which will be displayed in the computer program. After the initial stage, the sensor can detect the temperature/humidity information, and the transmitter can continuously send the data once every 10 s. A video of powering the transmitter and sensor is shown in Video S2, Supporting Information. Note that the distance of wireless transmission can reach tens to hundreds of meters.

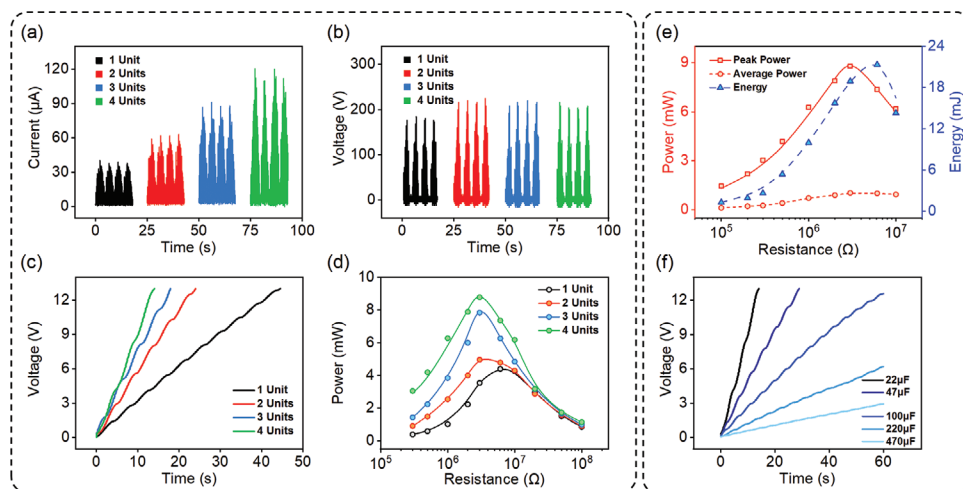


Figure 5. Output performance of the SSF-TENG array with four units under the water wave conditions of 10 cm and 1.1 Hz. a) Output current, b) output voltage for different TENG unit numbers. c) Charging voltage on a 22 μF capacitor for the SSF-TENG array with different unit numbers. d) Peak output power-resistance relationship for different SSF-TENG unit numbers. e) Peak power, average power-resistance relationships, and translated energy-resistance relationship for the four-unit SSF-TENG array. f) Charging voltage profiles on various capacitances for the four-unit SSF-TENG array.

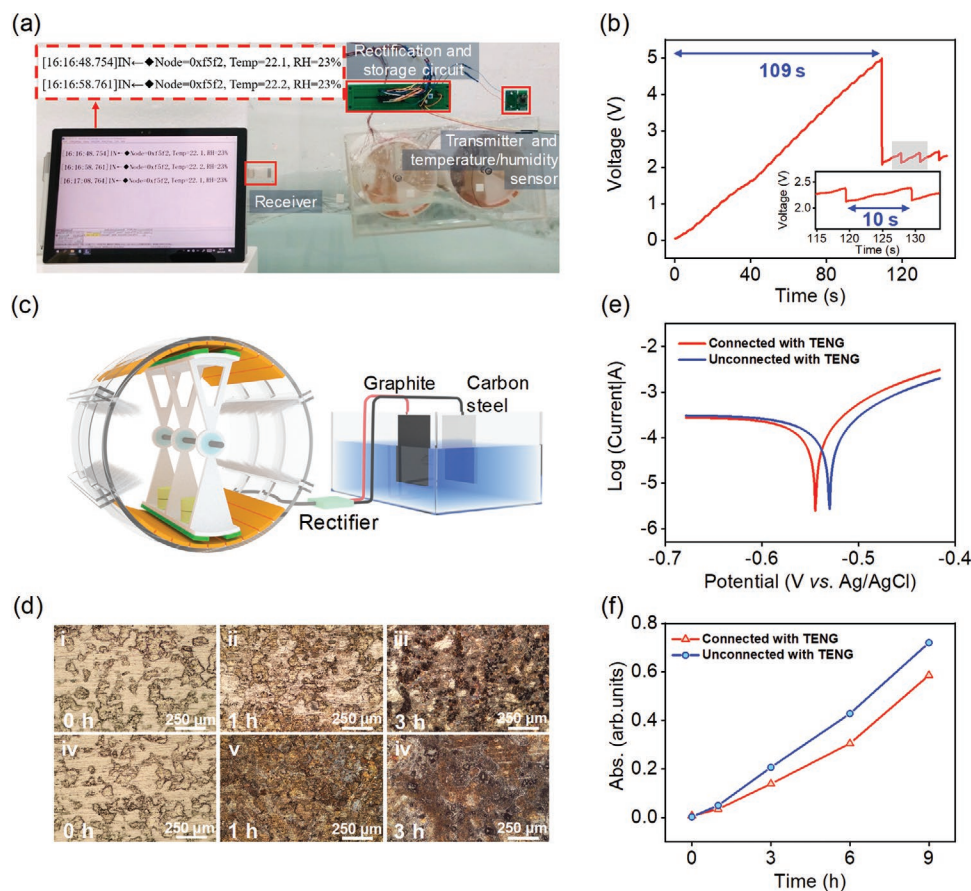


Figure 6. Demonstration of self-powered marine environmental application systems toward smart oceans. a) Photograph of the remote marine environmental information monitoring system driven by an array of four SSF-TENGs through the water wave energy harvesting. b) Charging and discharging processes of a 470 μF capacitor to drive the transmitter and temperature/humidity sensor. c) Schematic diagram of a simulated metal protection system. d) Optical photographs of Q235 carbon steel micro-areas, (i–iii) with SSF-TENG protection and (iv–vi) without SSF-TENG protection. e) Tafel curves of Q235 carbon steel with and without SSF-TENG protection. f) Absorption intensity of Fe^{3+} ions leached from NaCl solution.

Such transmitting and sensing systems can be placed in many positions for distributed detection, so as to build the internet of things on the ocean surface.

Metal corrosion caused by seawater is an important reason for shortening the lives of various offshore facilities and equipments, leading to great economic losses. The TENGs provide a self-powered solution of impressed current cathodic protection (ICCP).^[27–29] Figure 6c shows a schematic diagram of a simulated metal protection system powered by the SSF-TENG in a laboratory environment. A full-wave rectifier bridge was used to convert the alternating-current output of SSF-TENG to direct-current output, and the seawater environment was simulated by the NaCl solution with a mass fraction of 3.5%. The polished Q235 carbon steel (15 mm \times 25 mm \times 1 mm) and graphite sheet (10 mm \times 25 mm \times 1 mm) were immersed in the NaCl solution, which were used as the cathode and anode, respectively. Figure 6d and Figure S10, Supporting Information, show the macroscopic and microscopic optical photographs of Q235 carbon steel to visualize the inhibitory effect of metal protection system constructed by the SSF-TENG on its spontaneous corrosion in simulated seawater. The photographs of carbon steel micro-areas at different times with and without SSF-TENG protection are respectively presented in Figure 6d(i–iii), 6d(iv–vi).

It is apparent that the corrosion of carbon steel without SSF-TENG protection is more serious after 1 h and 3 h of immersion in NaCl solution. The Tafel curves in Figure 6e show that the potential of the protected carbon steel (-0.545 V vs Ag/AgCl) is more negative relative to the unprotected one (-0.530 V vs Ag/AgCl) during the spontaneous corrosion in 0.5 M Na_2SO_4 solution. In addition, Figure 6f shows that the protected carbon steel has a lower concentration of Fe^{3+} dissolved in the NaCl solution relative to the unprotected one at different stages, which again confirms the effectiveness of the metal corrosion protection system driven by the SSF-TENG.

In practice, such self-powered marine environmental application systems can be applied to offshore buoys and other marine equipments. When deploying the SSF-TENG arrays around or into the offshore equipments such as buoys to harvest ocean wave energy, the marine environmental information at this location can be collected and sent continuously as specified for a long period of time, and also the metal of offshore equipments can be protected against corrosion. For example, the marine hydrology, water quality, and meteorological data, especially the severe weather and sea state information, can be captured, which are required and essential for marine scientific research and offshore oil development, etc.

3. Conclusion

In summary, the output performance of swing-structured TENG was further optimized by using the flexible rabbit fur brushes and segmented structure. The influences of different segmented structures on the performance of as-fabricated SSF-TENG devices were explored, exhibiting the maximum output current of 74.0 μA under regular triggering, which is an 83.0% improvement over the unsegmented structure. By using ultra-lubricated ceramic bearings, the swing time after one triggering was further extended to exceed 5 min. Moreover, under the water wave triggering of 1.1 Hz and 10 cm, the SSF-TENG can deliver a maximum peak power of 6.2 mW and an average power of 0.74 mW, with enhancements of 11.1 and 7.0 times, respectively. Then the output characteristics of the SSF-TENG array were measured and found to be controlled by the unit number. Finally, self-powered marine environmental application systems, including remote marine environmental information monitoring and metal protection systems, were demonstrated through harvesting the water wave energy by the SSF-TENG or array, indicating that the TENGs have broad application prospects for large-scale collection of blue energy and the realization of smart oceans.

4. Experimental Section

Fabrication of the SSF-TENG Device: First, UV-curable resins were used to fabricate the cylindrical shell of the SSF-TENG (length: 20 cm, outer diameter: 15 cm, thickness: 3 mm), by the 3D printing technology. Four hollow strips of 19 cm in length and 3 mm in width, which were protruding for 10 mm from the shell, were designed for inserting the rabbit fur brushes of 18 cm in length and 3 mm in width. Then, two acrylic disks with circular holes of 17 mm, embedded by ultra-lubricated ceramic bearings with an inner diameter of 6 mm and an outer diameter of 17 mm, were made by laser cutting machine to be added on both ends of the shell. Third, a 3D-printed swing component with three connected-sector blocks (embedded with bearings) and two arc-shaped strips, was assembled with the shell through a steel shaft with a diameter of 6 mm and bearings in the bottom disks. The segmented structure of the swing component was expressed by the alternate appearance of protuberant and concave parts. When adjusting the grating number N of the swing component, the total central angle of its arc-shaped parts was fixed as 30° . The PTFE films were adhered to the protuberant surfaces having the matched sizes with complementary electrodes fabricated by the PCB technology. The gap between each copper electrode unit was 1 mm when the grating number N was 1, 2, while the gap was 0.5 mm when $N = 3, 4$. At different N , the total electrode area of 218.5 cm^2 remained unchanged. For larger swing components with the same effective tribo-surface area, the fabrication method was similar. After sealing and waterproofing the SSF-TENG with polymer glues, it was placed in the water for measuring its performance under the water wave triggering. In addition, to maintain synchronous movement of the SSF-TENG units in the array, an acrylic shell with a dimension of 67.5 cm \times 36.5 cm \times 19.5 cm was made to accommodate the array.

Electric Measurements of the TENG Device: The triggering equipment of the SSF-TENG includes a linear motor and a water wave generator. The working principle of the water wave generator was to realize water waves with different frequencies by controlling the motion of push plate with a programmable digital controller.^[23] A Keithley 6517B System Electrometer was employed for measuring the output current and transferred charge of the SSF-TENG as well as the capacitor voltage, while a Tektronix 3104 Mixed Domain Oscilloscope was used to measure

the output voltage. The performances of the simulated metal protection system driven by the SSF-TENG were measured on an electrochemical workstation in a three-electrode system (CHI 660E). Q235 carbon steel (15 mm \times 25 mm \times 1 mm) served as the working electrode, while the platinum foil (10 mm \times 20 mm \times 0.1 mm) and Ag/AgCl electrodes served as counter and reference electrodes, respectively.

Supporting Information

Supporting Information is available from the Wiley Online Library or from the author.

Acknowledgements

H.P. and Y.F. contributed equally to this work. Support from the National Key R & D Project from Minister of Science and Technology (2016YFA0202704), National Natural Science Foundation of China (Grant Nos. 51432005, 51702018, and 51561145021), and Youth Innovation Promotion Association, CAS, are appreciated. The authors also thank Xi Liang and Pinjing Lu for device fabrications and measurements.

Conflict of Interest

The authors declare no conflict of interest.

Data Availability Statement

Research data are not shared.

Keywords

blue energy, smart ocean, triboelectric nanogenerators, water wave energy harvesting

Received: July 3, 2021

Revised: August 10, 2021

Published online:

- [1] H. L. van Soest, M. G. J. den Elzen, D. P. van Vuuren, *Nat. Commun.* **2021**, *12*, 2140.
- [2] Z. L. Wang, *Nature* **2017**, *542*, 159.
- [3] Y. Bai, L. Xu, C. He, L. Zhu, X. Yang, T. Jiang, J. Nie, W. Zhong, Z. L. Wang, *Nano Energy* **2019**, *66*, 104117.
- [4] A. von Jouanne, *Mech. Eng.* **2006**, *128*, 24.
- [5] R. Henderson, *Renewable Energy* **2006**, *31*, 271.
- [6] M. T. Rahman, S. M. S. Rana, M. Salauddin, P. Maharjan, T. Bhatta, J. Y. Park, *Adv. Energy Mater.* **2020**, *10*, 1903663.
- [7] Y. Shi, F. Wang, J. Tian, S. Li, E. Fu, J. Nie, R. Lei, Y. Ding, X. Chen, Z. L. Wang, *Sci. Adv.* **2021**, *7*, eabe2943.
- [8] S. A. Graham, B. Dudem, H. Patnam, A. R. Mule, J. S. Yu, *ACS Energy Lett.* **2020**, *5*, 2140.
- [9] B. Dudem, N. D. Huynh, W. Kim, D. H. Kim, H. J. Hwang, D. Choi, J. S. Yu, *Nano Energy* **2017**, *42*, 269.
- [10] Z. L. Wang, T. Jiang, L. Xu, *Nano Energy* **2017**, *39*, 9.
- [11] L. Xu, T. Jiang, P. Lin, J. J. Shao, C. He, W. Zhong, X. Y. Chen, Z. L. Wang, *ACS Nano* **2018**, *12*, 1849.
- [12] Z. L. Wang, *Mater. Today* **2017**, *20*, 74.

- [13] Z. L. Wang, *Nano Energy* **2020**, *68*, 104272.
- [14] F.-R. Fan, Z.-Q. Tian, Z. L. Wang, *Nano Energy* **2012**, *1*, 328.
- [15] X. Ma, S. Li, S. Dong, J. Nie, M. Iwamoto, S. Lin, L. Zheng, X. Chen, *Nano Energy* **2019**, *66*, 104090.
- [16] S. Li, Y. Fan, H. Chen, J. Nie, Y. Liang, X. Tao, J. Zhang, X. Chen, E. Fu, Z. L. Wang, *Energy Environ. Sci.* **2020**, *13*, 896.
- [17] S. Li, J. Nie, Y. Shi, X. Tao, F. Wang, J. Tian, S. Lin, X. Chen, Z. L. Wang, *Adv. Mater.* **2020**, *32*, 2001307.
- [18] Y. Zi, H. Guo, Z. Wen, M.-H. Yeh, C. Hu, Z. L. Wang, *ACS Nano* **2016**, *10*, 4797.
- [19] M. Xu, T. Zhao, C. Wang, S. L. Zhang, Z. Li, X. Pan, Z. L. Wang, *ACS Nano* **2019**, *13*, 1932.
- [20] X. Yang, L. Xu, P. Lin, W. Zhong, Y. Bai, J. Luo, J. Chen, Z. L. Wang, *Nano Energy* **2019**, *60*, 404.
- [21] W. Zhong, L. Xu, X. Yang, W. Tang, J. Shao, B. Chen, Z. L. Wang, *Nanoscale* **2019**, *11*, 7199.
- [22] T. Jiang, H. Pang, J. An, P. Lu, Y. Feng, X. Liang, W. Zhong, Z. L. Wang, *Adv. Energy Mater.* **2020**, *10*, 2000064.
- [23] Z. Lin, B. Zhang, H. Guo, Z. Wu, H. Zou, J. Yang, Z. L. Wang, *Nano Energy* **2019**, *64*, 103908.
- [24] P. Chen, J. An, S. Shu, R. Cheng, J. Nie, T. Jiang, Z. L. Wang, *Adv. Energy Mater.* **2021**, *11*, 2003066.
- [25] J. An, Z. M. Wang, T. Jiang, X. Liang, Z. L. Wang, *Adv. Funct. Mater.* **2019**, *29*, 1904867.
- [26] X. Liang, T. Jiang, Y. Feng, P. Lu, J. An, Z. L. Wang, *Adv. Energy Mater.* **2020**, *10*, 2002123.
- [27] W. Wang, Y. Wu, Z. Chang, F. Chen, H. Wang, G. Gu, H. Zheng, G. Cheng, Z. L. Wang, *ACS Appl. Mater. Interfaces* **2019**, *11*, 6396.
- [28] Y. Feng, Y. Zheng, Z. U. Rahman, D. Wang, F. Zhou, W. Liu, *J. Mater. Chem. A* **2016**, *4*, 18022.
- [29] Y. Feng, T. Jiang, X. Liang, J. An, Z. L. Wang, *Appl. Phys. Rev.* **2020**, *7*, 021401.